Symmetry Breaking in Monometallic Nanocrystals toward Broadband and Direct Electron Transfer Enhanced Plasmonic Photocatalysis

Wei Shao, Qianqian Pan, Qiaoli Chen, Chongzhi Zhu, Weijian Tao, Haiming Zhu, Huijun Song, Xuelu Liu, Ping-Heng Tan, Guan Sheng, Tulai Sun, Xiaonian Li, and Yihan Zhu*

Metallic nanocrystals manifest themselves as fascinating light absorbers for applications in plasmon-enhanced photocatalysis and solar energy harvesting. The essential challenges lie in harvesting the full-spectrum solar light and harnessing the plasmon-induced hot carriers at the metal–acceptor interface. To this end, a cooperative overpotential and underpotential deposition strategy is proposed to mitigate both the challenges. Specifically, by utilizing both ionic additive and thiol passivator to introduce symmetry-breaking growth over gold icosahedral nanocrystals, the microscopic origin can be attributed to the site-specific nucleation of stacking faults and dislocations. By adopting asymmetric crystal shape and unique surface facets, such nanocrystals attain high activity toward photocatalytic ammonia borane hydrolysis, arising from combined broadband plasmonic properties and enhanced direct transfer of hot electrons across the metal–adsorbate interface.

1. Introduction

Metallic nanocrystals are endowed with highly flexible geometries,[1] broadly tunable optical properties,[2] and catalytically

Dr. W. Shao, Q. Pan, Dr. Q. Chen, C. Zhu, H. Song, Dr. T. Sun, Prof. X. Li, Prof. Y. Zhu
Center for Electron Microscopy
State Key Laboratory Breeding Base of Green Chemistry Synthesis Technology and College of Chemical Engineering
Zhejiang University of Technology
Hangzhou 310014, China
E-mail: yihanzhu@zjut.edu.cn
W. Tao, Prof. H. Zhu
Centre for Chemistry of High-Performance and Novel Materials
Department of Chemistry
Zhejiang University
Hangzhou, Zhejiang 310027, China
X. Liu, Prof. P.-H. Tan
State Key Laboratory of Superlattices and Microstructures
Institute of Semiconductors
Chinese Academy of Sciences
Beijing 100083, China
G. Sheng
Advanced Membranes and Porous Materials Center
Physical Science and Engineering
King Abdullah University of Science and Technology
Thuwal 23955-6900, Kingdom of Saudi Arabia

The ORCID identification number(s) for the author(s) of this article can be found under https://doi.org/10.1002/adfm.202006738.

active surfaces.[3] One of their most attractive optical properties is surface plasmon resonance (SPR), which is closely associated with the coherent oscillations of conduction electrons coupled with incident electromagnetic field.[4] SPR is reported to dramatically enhance the optical absorption and scattering cross-sections of the metallic nanocrystals and enables a wide range of applications related with nonlinear optical spectroscopy (e.g., surface-enhanced Raman scattering)[5] as well as plasmon-enhanced photovoltaics and photocatalysis.[6] To involve a photochemical reaction, the resonant excitation of surface plasmons over the metallic nanocrystals dephases and generates highly energetic but short-lived hot carriers either in metals or among the hybridized states located at metals and strongly interacting adsorbates/semiconductors, respectively.[6d,7] The former dephasing pathway allows the indirect interfacial transfer of electrons carrying sufficient energy from metals to the electron-accepting orbitals of contacted adsorbates/semiconductors, followed by the thermalization through electron–electron and electron–phonon scattering.[8] The latter leads to more efficient direct interfacial electron transfer through chemical interface damping (CID),[7a,9] which significantly retards the relaxation of hot carriers either by chemical interface scattering (CIS) at metal/adsorbate interface[10] or Schottky barrier at the metal/semiconductor interface.[11] The injected hot electrons subsequently participate in the photochemical reactions with slow kinetics via either vibrationally excited "hot adsorbates" or energy-level adjustable conduction band (CB) of semiconductors.[10–12] Interestingly, the competition between different plasmon dephasing pathways and thus the overall photocatalytic performance of metallic nanocrystals critically relies on their size and shape,[3,13] the precise chemical synthesis of metallic nanocrystals, and fundamental understanding of corresponding growth mechanisms are therefore the prerequisites for the design and discovery of high-performance plasmonic photocatalysts.[14]

The advances in wet-chemical synthesis of metallic nanocrystals have led to a significant outburst of researches focused on the precise structural and morphological control of colloidal metallic nanocrystals that even adopt a high degree of structural complexity.[15] Among these studies, the synthesis of metallic nanocrystals with reduced symmetry (RS) and the

investigation of associated symmetry-breaking growth mechanisms are of great significance and challenge, because the equilibrium crystal shape (ECS) is predominantly dictated by the point group symmetry of crystal structures and restricted by the surface energy based on Wulff theorem.[16] Breaking this symmetry leads to vast unique plasmonic properties including Fano resonance,[17] broadband absorption,[18] and local-field enhancement.[17a] Despite the extensive studies and robust theory on crystal growth,[19] the synthesis of metallic nanocrystals with reduced symmetry remains nontrivial through wet-chemical methods and is restricted to physical fabrication techniques like electron/ion beam etching, deposition, and lithography,[20] which considerably limits their synthetic scalability and thus practical applicability. There are scattered reports on the wet-chemical synthesis of monometallic nanocrystals with reduced symmetry either through precisely controlled growth kinetics,[1a,d,19a] ligand/metal additive modulated growth,[1d,20b,21] or hard template growth strategies.[19b,22] On the other hand, bimetallic nanocrystals provide more routes toward the symmetry-breaking growth via either the Fermi level or lattice mismatch between the two metal components.[23] Notwithstanding this, the precise structural engineering of such nanocrystals and the underlying microscopic symmetry-breaking growth mechanisms remain largely unexplored.

In this work, based on the defect-mediated symmetry-breaking growth mechanism, we proposed a cooperative overpotential and underpotential deposition (COUD) strategy over the gold icosahedral plasmonic nanocrystals. This is achieved by properly aligning the reduction potentials between Au and the alien ions, the latter of which would initiate the defect formation and associated symmetry-breaking growth. The cooperative underpotential deposition (UPD) of monovalent copper precursor and overpotential deposition (OPD) of thiol-passivated gold precursor on the surface of gold icosahedral seeds are followed by the simultaneous bulk co-deposition of gold/copper and galvanic displacement of copper, which result in the symmetry-breaking growth and lead to the formation of diamond shaped multiply-twinned (MT) gold nanocrystals. The microscopic mechanism is corroborated by combined electron microscopy and microanalysis, where the site-specific nucleation of stacking faults and dislocations initiates the symmetry-breaking growth. The as-synthesized nanocrystals exhibit broadband plasmonic absorption and high photocatalytic activity toward the ammonia borane decomposition reaction. Integrating the steady-state anti-Stokes Raman spectroscopy, transient absorption (TA) spectroscopy, and density-functional theory (DFT) calculations, we attribute the observed photocatalytic activity to not only the broadband optical properties but also the promoted direct interfacial transfer of hot electrons across the metal–adsorbate interface.

2. Results and Discussion

A promising strategy to introduce reduced symmetry in bimetallic nanocrystals is strain-mediated seeded growth,[23a] which allows the switching in growth modes among the conformal epitaxial Frank–van der Merwe (FM),[24] segregated epitaxial Volmer–Weber (VW),[25] and Stranski–Krastanov (SK)[26] modes by modulating the lattice mismatch between the seed and overgrown metal.[27] The overgrowth of monometallic nanocrystals cannot generate such a mismatched seed/overgrown layer interface, while symmetry-breaking growth in a nonepitaxial manner could be evoked by the ligand-induced inhomogeneous strain fields under slow reaction kinetics.[1d] We propose that a tandem deposition and galvanic displacement reaction of a secondary metal that adopt a large lattice mismatch with the seed could on one side introduce significant interfacial strain for initiating the symmetry-breaking growth in the intermediate structure and on the other side maintain the monometallic nature of the final nanocrystal. As a proof-of-concept study, copper as a secondary metal was hereby used to shape the gold nanocrystal with reduced symmetry because of the large Cu/Au lattice mismatch of 11.4% and galvanic displacement reaction between them. A practical difficulty lies in the far more negative reduction potential of Cu precursors than Au precursors, which prohibits the incorporation of Cu species into the Au nanocrystal at the early stage of seeded growth. To this end, a COUD strategy was used to mitigate the problem and manipulating their respective reduction potentials by simultaneously passivating the Au precursor and facilitating the Cu deposition onto the surface of Au seed, as schematically illustrated in **Figure 1**a. This concept is clearly evidenced by the cyclic voltammetry (CV) results (Figure 1b), which show that the passivation of $AuCl_4^-$ species by 4-mercaptophenol (4-MP) molecules significantly lowers the reduction potential of Au compared with its equilibrium potential by about 0.40 V and decreases the electrochemical current in the overpotential regime on a gold electrode. On the other hand, the $Cu(NH_3)_2^+$ species are used as the Cu(I) precursor and exhibit about 0.41 V more positive Cu(I) → Cu(0) reduction peak in the underpotential regime of the CV curve on a gold electrode (Figure 1b) than the reduction on a Cu electrode (Figure 1b). Actually, the UPD of Cu on Au surface is a widely observed phenomenon as reported before.[28] In this sense, the cooperative Cu UPD and Au OPD would allow the formation of a highly strained surface atomic layer incorporated by Cu atoms on the Au seed, which is then subjected to further deposition of Au atoms. The repetitive COUD steps could introduce large strain at the seed/overgrown layer interface through Cu deposition and the metallic Cu species would finally be displaced by Au (Figure 1a), both of which are critical factors for creating monometallic Au nanocrystals with reduced symmetry.

We applied the COUD strategy to the colloidal synthesis of Au nanocrystals with the assistance of both $Cu(NH_3)_2^+$ species and 4-MP thiol ligands. Instead of the conventional conformal seeded growth that leads to the formation of spherical Au nanocrystals, the COUD strategy allows the anisotropic growth toward the reduced symmetry diamond shaped Au (RS-Au) nanocrystals with a size about 10 nm (**Figure 2**). In order to explore the structural evolutions of such a symmetry-breaking growth, the reaction was quenched at different stages and the intermediates are investigated by high-angle annular dark-field scanning transmission electron microscopy (HAADF-STEM). According to Figure 2a–e, the anisotropic growth starts from the spherical Au seeds and features the eccentric shape evolution and site-specifically protruded island that finally evolve to the tip of the RS-Au nanocrystals. The atomic-scale structural evolution can be further investigated
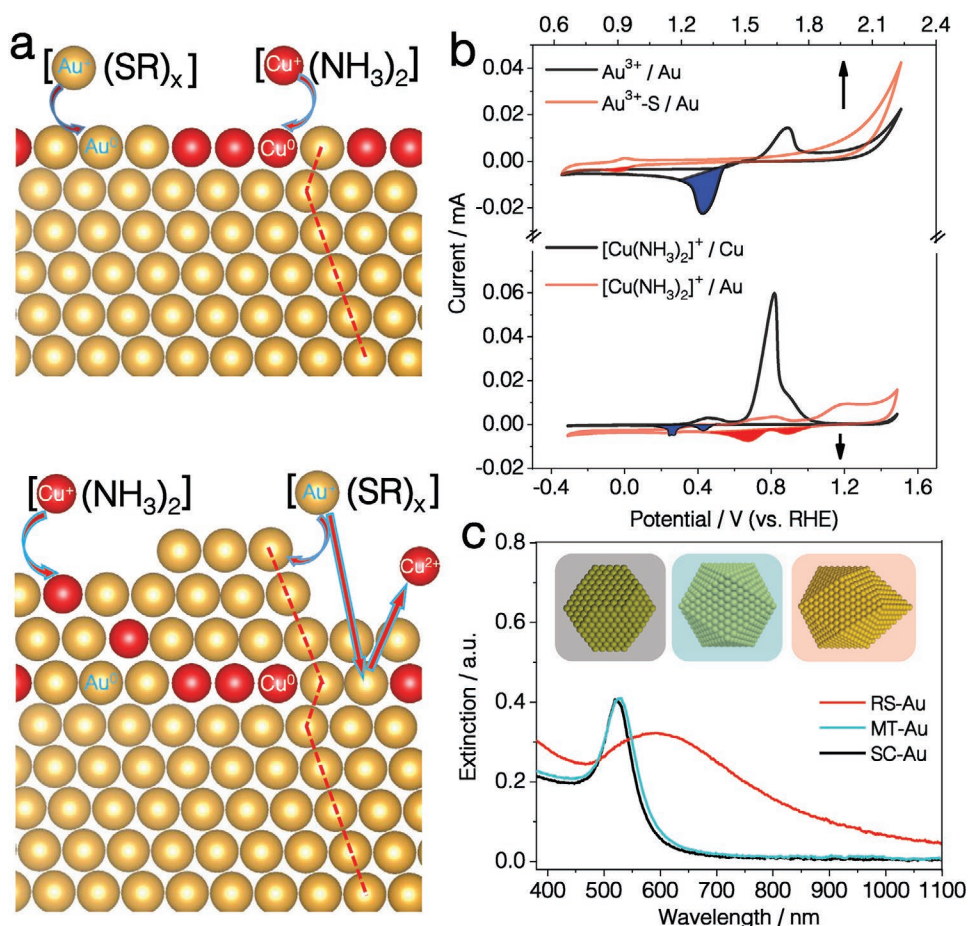
Figure 1. a) Schematic illustration of the COUD strategy for the synthesis of RS-Au nanocrystals (tandem deposition and galvanic displacement process). b) The upper figure compares CV curves of Au electrode measured in 0.5×10^{-3} M $HAuCl_4$ and 0.5×10^{-3} M $HAuCl_4 + 0.25 \times 10^{-3}$ M 4-MP mixture solution, respectively. The bottom figure compares CV curves of Cu electrode and Au electrode in 0.01 M $Na_2SO_4 + 0.01 \times 10^{-3}$ M $Cu(NH_3)_2^+$ mixture solution (scan rate: 5 mV s^{-1}), respectively. c) The extinction spectra of SC-Au, RS-Au, and MT-Au. The insets refer to the corresponding models of three crystal shapes.

by aberration-corrected STEM, which corroborates that the symmetry-breaking growth follows the nonepitaxial route and starts from a multiply-twinned icosahedral Au seed (**Figure 3**). The high-resolution (HR) STEM image and corresponding fast Fourier transform (FFT) of a key intermediate as shown in Figure 3a–f suggest that the protruding island is twinned with the spherical icosahedral nanocrystal and the interface is significantly strained as observed in a shear strain component by the geometric phase analysis (GPA) (Figure S1, Supporting Information). Additionally, an edge dislocation is also observed in the vicinity of the twin boundary marked by a red dashed line (Figure 3f). It is thus speculated that the incorporation of Cu by UPD during overgrowth introduces significant shear strain on the surface that has been reported to lower the stacking fault (SF) energy and facilitate the nucleation of SFs and nanotwins.[1d] Similar strain induced twinning and anisotropic overgrowth arising from Cu deposition has also been observed on an Au@Cu nanorod before.[23c] The continuous single-site anisotropic overgrowth of the icosahedral Au seed leads to a diamond shaped nanocrystal, of which the protruding island finally evolves to extra multiply-twinned tetrahedra extending

from the icosahedral nanocrystal composed of 20 tetrahedral units with a common vertex. Moreover, the evolution of chemical compositions over individual intermediate nanocrystals can also be tracked by energy-dispersive X-ray spectroscopy (EDS) mapping during the symmetry-breaking growth (Figure 2a–e), which exhibits gradually decreased Cu concentration and is quantitatively verified by atomic absorption spectroscopy (AAS) (Figure 2g, i.e., from 1.6 to 0.6 wt%). This confirms that traces of Cu as the secondary metal that initiates the symmetry-breaking growth of monometallic Au nanocrystal are fully involved in the tandem deposition and galvanic displacement process. Notably, we found that the overgrowth behavior strongly depends on the types of Cu precursors and the Cu(II) species (i.e., $Cu(NH_3)_4^{2+}$) would however introduce multisite overgrowth that finally lead to the formation of flower-like nanocrystals (Figure S2, Supporting Information). Considering the fact that the Cu(II) species exhibit a more positive reduction potential and high electrochemical current than that of the Cu(I) species (Figure S3, Supporting Information), such a difference in overgrowth behavior may originate from the distinct deposition rate of Cu atoms in these two separate cases: the Cu(I) precursor features
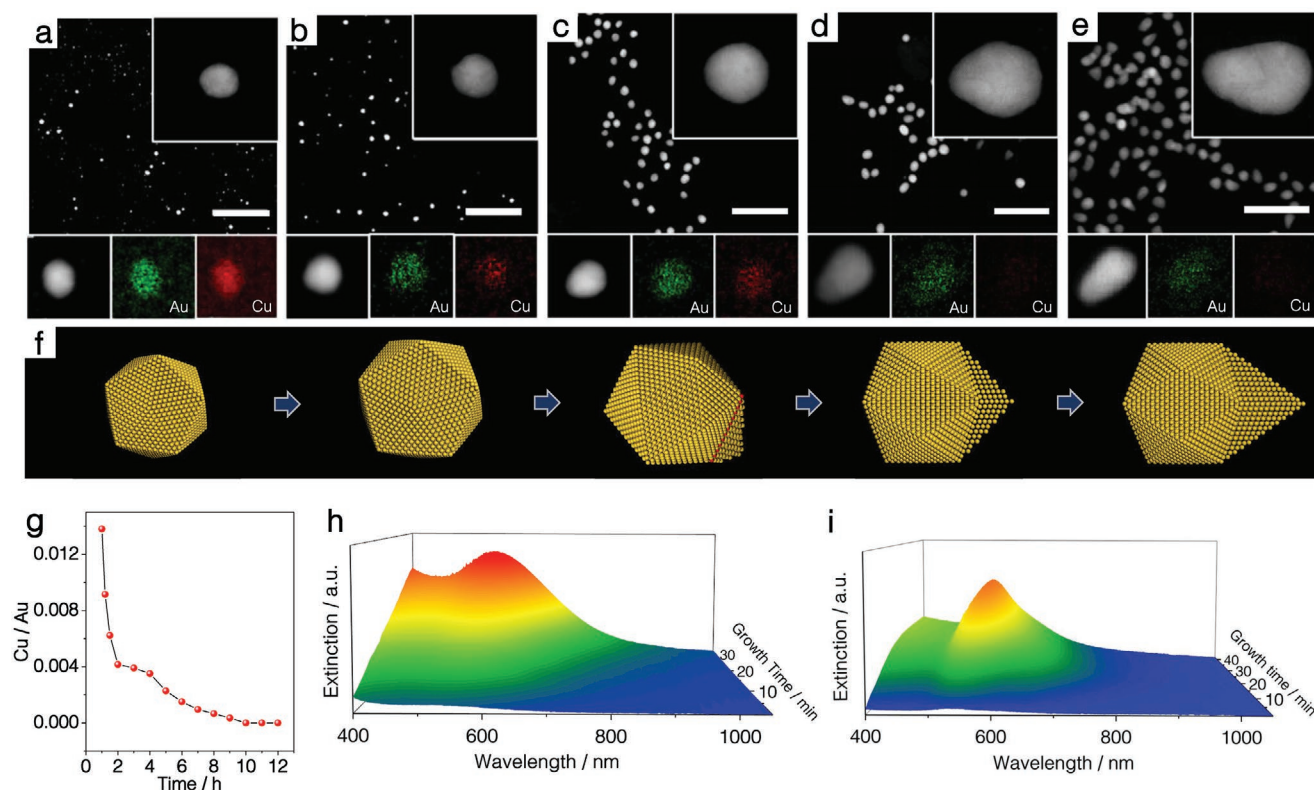
Figure 2. a–e) HAADF-STEM images and EDX-elemental mappings of the intermediates collected at different growth stages of RS-Au: a) 5 s, b) 1 min, c) 2 h, d) 6 h, and e) 12 h. The upper right insets show magnified HAADF-STEM images of individual nanocrystals, respectively. Scale bar: 50 nm. f) The corresponding atomic structure models at respective stages of the symmetry-breaking growth process of RS-Au nanocrystals. g) The elemental mass ratio of Cu/Au at different reaction stages. h,i) In situ UV–vis extinction spectra of early stage growth dynamics for Au nanocrystals with and without Cu(I) ion additives, respectively.

the slow and site-selective Cu UPD onto the energetically most favorable site, and thus allows the single-site anisotropic overgrowth; the Cu(II) precursor features fast and nonsite-selective Cu UPD and results in multisite overgrowth. This point is further confirmed by tracking the chemical compositions of the intermediates during overgrowth using Cu(II) precursor, which shows in nanocrystals a much higher concentration of Cu that cannot be efficiently displaced by Au (Figure S4, Supporting Information). On the basis of the above observations and analysis, we try to propose an atomic-scale symmetry-breaking growth mechanism via the COUD strategy as follows. The site-selective surface deposition of a Cu incorporated UPD layer initiates the strain-induced single-site nucleation of a mis-stacked atomic layer. This is followed by the successive anisotropic overgrowth through nanotwinning and a galvanic displacement step, toward the shaping of monometallic nanocrystals with reduced symmetry.

In principle, the extended multiply-twinned tetrahedra from the {111} facets of an icosahedral Au seed through a nonepitaxial manner (i.e., twinning) would terminate as {100} facets in order to form a smooth surface with minimized surface curvature (Figure 3h). In addition, there remains a 2.9° solid-angle deficiency for the two neighboring tetrahedral units overgrown from the icosahedron as schematically illustrated in Figure 3h, which could be accommodated by large elastic strain. Similar phenomenon can be observed in multiply-twinned decahedral

nanocrystals that contain a 7.35° solid-angle deficiency accommodated by combined disclination and shear strain.[29] Accordingly, we use the second nearest-neighbor modified-embedded atom method (MEAM) potential to optimize the geometries of both Au icosahedron and RS-Au nanocrystal (≈8 nm size), which are subject to the quantification of strain distribution via mean interatomic distances with respect to the bulk Au–Au nearest neighbor distance. As shown in the excavated nanocrystal models (Figure 3g), the Au icosahedron has enriched tensile surface strain up to 1.22%, closely resembling the observed strain distribution of Pt icosahedral nanocrystals.[30] While the RS-Au nanocrystals exhibit markedly enhanced tensile strain (up to 1.51%) at the interface between the {111} terminated icosahedron and {100} terminated twin-tetrahedral units. These points can be further verified by calculating the component-specific pair distribution function (PDF) profiles of both models as shown in Figure 3g,h, where the surface and/or interface are enriched with tensile strain by adopting a larger Au–Au interatomic distance. The proposed structural model of the RS-Au nanocrystal made of a {111} faceted icosahedron capped with {100} faceted twin-tetrahedral units can be validated by HRSTEM imaging upon two distinct zone axes as shown in Figure 3a,b. From projections close to the [112] and [110] axes of two randomly chosen nanocrystals, respectively, both experimental HRSTEM image and FFT pattern match well with the simulated ones based on the proposed
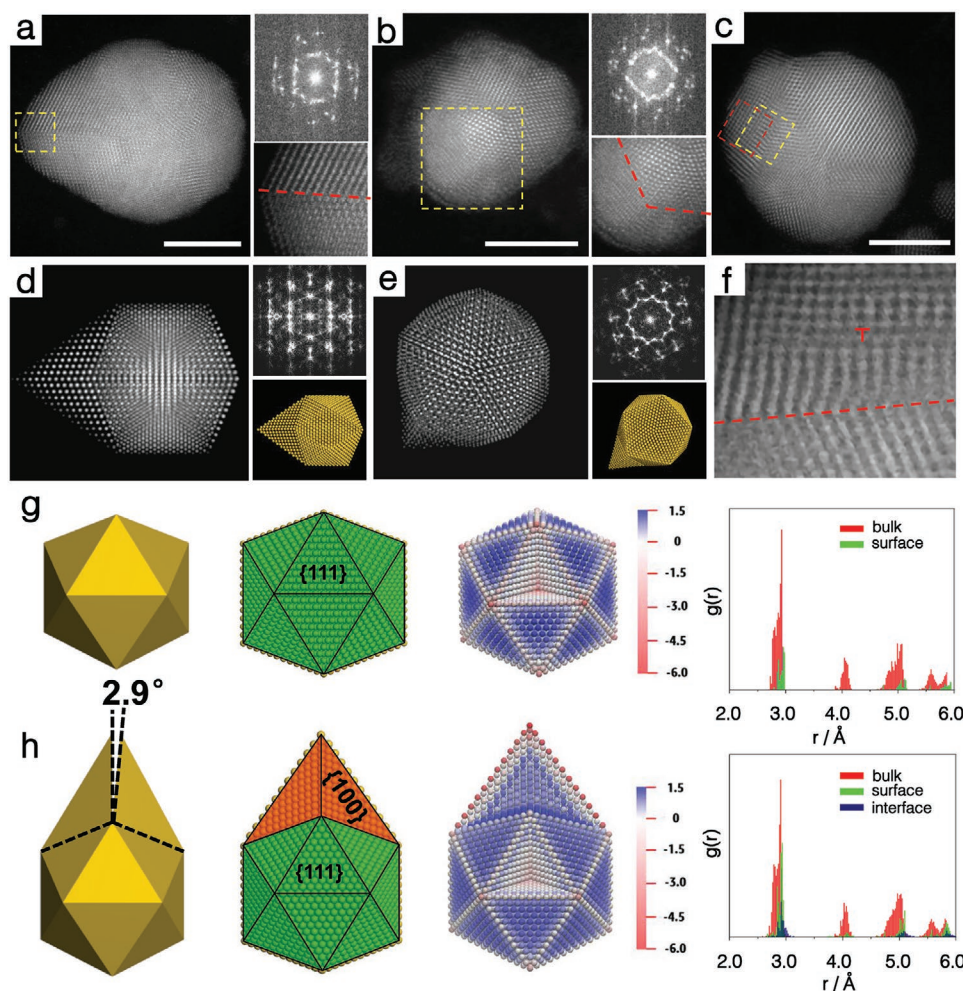
Figure 3. HAADF-STEM images of two randomly chosen RS-Au nanocrystals projected close to a) [112] and b) [110] directions, respectively. The upper and lower right insets refer to corresponding FFT patterns and magnified image of the area marked with yellow dashed square. Scale bar: 5 nm. c) HAADF-STEM image of an intermediate structure for RS-Au nanocrystal collected at 1 min. The areas marked with red and yellow dashed squares are used for strain analysis and an enlarged view in shown in (f), respectively. Scale bar: 5 nm. STEM image simulation of RS-Au nanocrystals projected along d) [112] and e) [110] directions. The upper and lower right insets refer to corresponding FFT patterns and atomic structure models. From left to right, polyhedral model, facet-decorated polyhedral model, strain-embedded atomic structure model (strain amplitude rendered by the color bar, in %), and PDF profiles for g) Au icosahedral and h) RS-Au nanocrystals.

structural model for the RS-Au nanocrystal (Figure 3d,e). The twin boundaries between the twin-tetrahedral units and moreover between these units and icosahedral seed can be clearly visualized from these projections, respectively (marked by red dashed lines).

One attractive optical feature for such metallic nanocrystals with reduced symmetry is broadband plasmonic properties, originating from either SPR mode splitting[19b] or selection rule relaxation.[17a] The as-synthesized RS-Au nanocrystals exhibit broadband plasmonic properties extending from visible to near-infrared region according to the UV–vis spectra in Figure 1c, which is distinct from the narrowband optical properties (i.e., a SPR peak centered at ≈530 nm) of spherical nanocrystals with either a single-crystalline (SC-Au) or multiply-twinned (MT-Au) structure. The in situ UV–vis spectra allows the monitoring of structural dynamics during crystal growth, which exhibits a time-dependently broadened extinction band and

corresponds to the anisotropic overgrowth of Au icosahedral seeds with the Cu(I) additive (Figure 2h). Without such an additive, the dynamic SPR band broadening is not observed during the overgrowth and spherical Au nanocrystals are derived (Figure 2i; TEM image is shown in Figure S5 in the Supporting Information). The broadband plasmonic properties of the Au nanocrystals allow the efficient light harvesting, which enable the plasmon-enhanced photocatalysis and hot carrier mediated photochemical reactions.

The phototriggered ammonia borane (AB) hydrolysis was chosen as a probe reaction to evaluate the photocatalytic properties of RS-Au. As shown in **Figure 4**b, the colloidal RS-Au nanocrystals completed the photocatalytic hydrolysis of AB (0.1 mmol, H_2/AB ratio = 3) much faster than either SC-Au (TEM image is shown in Figure S6 in the Supporting Information) or MT-Au (TEM image is shown in Figure S7 in the Supporting Information) nanocrystals exchanged with 4-MP thiol ligands, under the
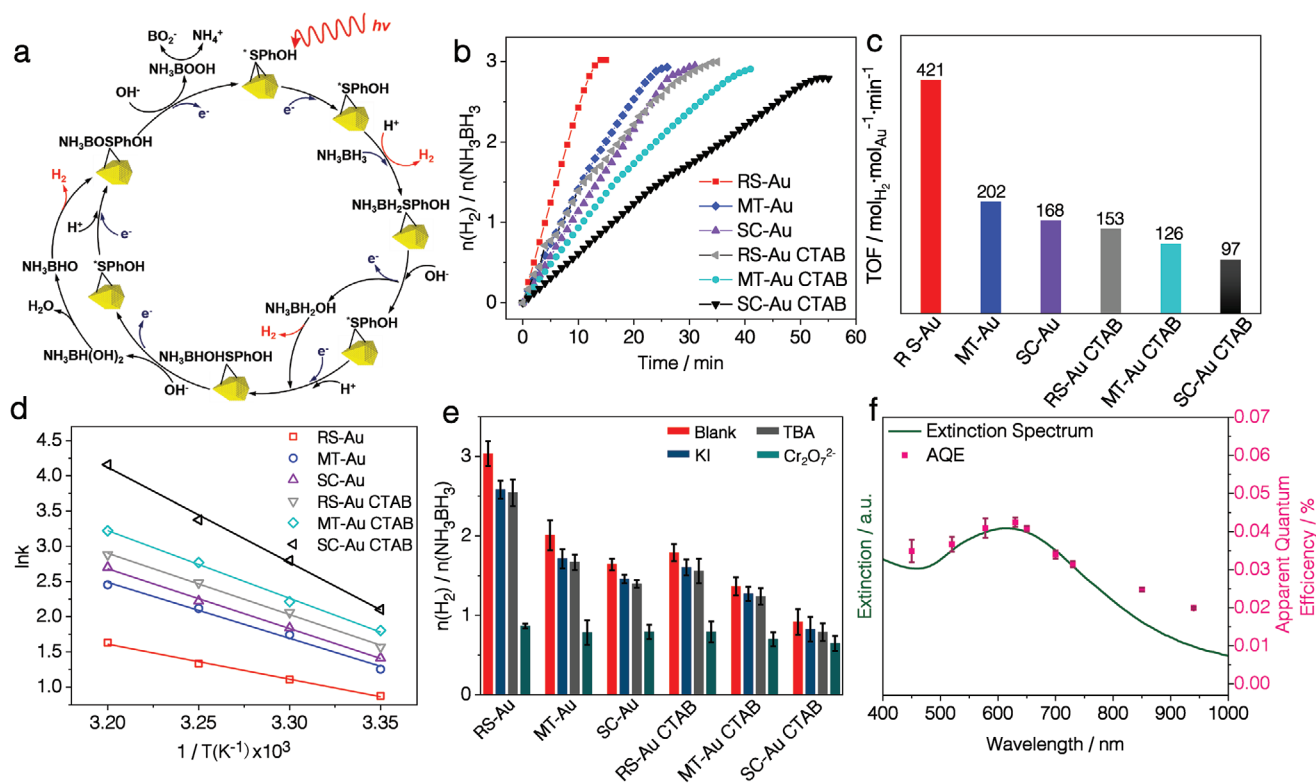
Figure 4. a) The proposed mechanism of hot electron-driven photocatalysis of AB hydrolysis, modified from a reported thermal catalysis mechanism.[48] Those routes that produce three molar equivalents of H_2 relative to AB molecules are rendered in red color. b) Time dependent molar ratio of produced H_2 to AB molecules, c) the calculated TOF values, and d) Arrhenius plots. e) Molar ratio of produced H_2 to AB molecules scavenged by electron, hole, and radical scavengers at 15 min for RS-Au, MT-Au, and SC-Au nanocrystals exchanged with either 4-MP or CTAB ligands. f) The measured wavelength-dependent apparent quantum efficiency for H_2 evolution compared with the extinction cross-section of RS-Au nanocrystals.

irradiation of a Xenon lamp. The calculated turnover frequency (TOF) values for RS-Au, MT-Au, and SC-Au nanocrystals are 421, 202, and 168 mol_{H_2} mol_{Au}^{-1} min^{-1}, respectively (Figure 4c). Blank (catalyst-free) and dark reactions show negligible reactivity for all nanocrystals (Figure S8, Supporting Information). Kinetic studies as shown in Figure 4d and Figure S9 in the Supporting Information further revealed a much lower apparent activation energy of 41.3 kJ mol^{-1} for RS-Au nanocrystals than the other two samples of SC-Au (70.6 kJ mol^{-1}) and MT-Au (67.7 kJ mol^{-1}). Interestingly, we note that the types of capping ligands of these colloidal nanocrystals play a significant role in determining their overall photocatalytic activity. This arises from the fact that after exchanging the thiol ligands by CTAB molecules, the TOF values of these nanocrystals drop significantly to 153 (RS-Au CTAB), 126 (MT-Au CTAB), and 97 (SC-Au CTAB) mol_{H_2} mol_{Au}^{-1} min^{-1}, respectively. The complete ligand exchange is achieved by repeated incubation using concentrated CTAB solution and can be verified by Fourier transform infrared spectroscopy (FTIR) spectra as shown in Figure S10 in the Supporting Information, which exhibit diminished vibrational peaks characterized for 4-MP molecules and dominant vibrational peaks for CTAB molecules after the ligand exchange. The RS-Au also shows excellent recyclability; the photocatalysis ability maintains within 5 cycles (Figure S11, Supporting Information). By further quenching the photochemical reaction by either electron, hole, or radical scavengers, respectively

(i.e., $Cr_2O_7^{2-}$, KI, and *tert*-butyl alcohol (TBA)), we confirm that hot electrons are the major carriers involved in the photochemical reaction since a most prominent drop in photocatalytic activity was observed when hot electrons rather than hot holes or radicals are scavenged (Figure 4e; Figure S12, Supporting Information), which is in accordance with Au/TiO_2 system.[31] Furthermore, we have conducted the activity test of RS-Au at different temperatures without light irradiation. With increased temperature from 25 to 40 °C, the $n(H_2)/n(AB)$ of RS-Au slightly increases from 0.30 to 0.71 at a reaction time of 15 min, which is much lower than the case with light irradiation (Figure S13, Supporting Information). The above facts indicate that the current photocatalytic reaction is mainly contributed by hot electron transfer processes. This result also coincides with the observation that the temperature rise for a RS-Au colloidal solution under light irradiation is comparable with that of pure water (Figure S14, Supporting Information) and the well documented fact that the photothermal effects are less pronounced in smaller metallic nanocrystals.[32]

Taken together, the RS-Au nanocrystals with broadband plasmonic properties exhibit promising photocatalytic activity and strongly interacting adsorbates like thiols that chemically bond with the Au surface would provide more efficient interfacial hot electron transfer than those weakly adsorbed molecules. It is speculated that the enhanced photocatalytic activity of RS-Au nanocrystals may be contributed by anisotropic near-field

enhancement arising from the asymmetric shape according to the finite-difference time domain (FDTD) simulations (Figure S15, Supporting Information), because the strong field enhancement at the tip of RS-Au nanocrystals could facilitate the electron–hole separation.[33] Notwithstanding this, a significant decrement in activity caused by ligand exchange indicates a more pronounced effect from ligand-induced interfacial hot electron transfer. An unexpected observation is related with the wavelength dependent measurement of apparent quantum efficiency (AQE) over RS-Au nanocrystals using band pass filters ranging from 450 to 940 nm with a spacing of 50 nm and under a normalized power density of 40 mW cm^{-2}. The wavelength dependence of AQE in Figure 4f fits well with the extinction of the RS-Au nanocrystals below 730 nm but exhibits a marked elevation above this wavelength. The plasmon-enhanced photocatalytic AQE is directly related with efficiency of electron transfer across the plasmonic metal/adsorbate interfaces as reported by Xiong and co-workers.[34] For metal/adsorbate interfaces dominated by indirect electron transfer, an optimum efficiency is achieved under the resonant condition of metal SPR and a good match between AQE and SPR extinction cross-section is usually expected[34] as observed for MT-Au and SC-Au nanocrystals (Figure S16, Supporting Information). The direct electron transfer through CID would require in addition an energy match with highest occupied molecular orbital (HOMO)–lowest unoccupied molecular orbital (LUMO) transition of hybridized surface states from adsorbates, of which an optimum efficiency is usually achieved at the longer wavelength than the resonant energy of HOMO–LUMO gaps for free-standing molecules.[35] The largely broadened SPR bands in the extinction spectra may also be contributed by CID in addition to the effects from the asymmetric shape of RS-Au nanocrystals, as the CTAB exchanged nanocrystals exhibit narrowed SPR bands compared with the 4-MP capped ones (Figure S17, Supporting Information). To evaluate the overall effects of the ligands on the photogenerated carriers, we conducted the AB hydrolysis reactions over RS-Au nanocrystals bonded with different types of thiol ligands. Actually, it has been reported that the CID pathway is well tunable by different types of ligands.[36] To this end, we exchange four types of thiol ligands with similar molecular structures but different substituents on a benzene ring onto the surface of RS-Au nanocrystals, including 4-MP with a *para* −OH group, 4-nitrothiophenol (4-NTP) with a *para* −NO$_2$ group, 4-mercaptobenzoic acid (4-MBA) with a *para* −COOH group, and 4-aminothiophenol (4-ATP) with a *para* −NH$_2$ group. As shown in Figure S18 in the Supporting Information, the extinction spectra of surface exchanged RS-Au colloidal solution exhibit different degrees of plasmon peak broadening and red-shift, which are characterized for the CID effects. The corresponding order in CID enhancement coincides well with the literature.[36] Interestingly, RS-Au nanocrystals exchanged with these four types of thiol ligands exhibit quite different activity toward the H$_2$ production, which clearly indicates that ligands play a key role in the hydrolysis of AB molecules. Moreover, the activity exactly follows the order of CID enhancement as 4-NTP > 4-MBA > 4-MP > 4-ATP, which unambiguously demonstrates that the direct electron transfer mediated by CID pathway dominates the reaction activity. Moreover, the observed linear power dependence of reaction rates (i.e., TOF values) for RS-Au

nanocrystals is associated with single carrier excitation events (Figure S19, Supporting Information),[37] and in some cases regarded as a signature for the direct rather than the indirect charge transfer pathway.[38] The latter usually holds a superlinear power dependence of reaction rates.[37] Accordingly, the above observations for the RS-Au photocatalyst strongly indicate the involvement of direct interfacial electron transfer events.[38b]

To further prove this point, we performed steady-state anti-Stokes and Stokes Raman spectroscopy on these Au nanocrystals, since Raman scattering, either in the Stokes or anti-Stokes regimes, is a unique spectral fingerprint of vibrations in the molecules through inelastic light-scattering.[39] The measurement of both Stokes and anti-Stokes scattering spectra allows the evaluation of the steady-state charge exchange with the vibrationally excited molecules through the determination of vibrational temperatures of both plasmonic nanocrystals and adsorbates (**Figure 5**b).[9b,40] Specifically, the equilibrated electron–phonon temperature of these plasmonic Au nanocrystals can be calculated through the Fermi–Dirac distribution function. By fitting the intensity of the anti-Stokes background signal to Equation (S2) in the Supporting Information, the local nanoparticle temperatures of RS-Au, MT-Au, and SC-Au are quite similar as shown in Figure 5c (details in Figure S20 and Equations (S2)–(S4) in the Supporting Information), which are higher than the ambient temperature due to the local heating by laser irradiation. On the other side, the transient metal/adsorbate interfacial electron transfer and associated vibronic coupling allows the heating of adsorbates and their vibrational temperature can be calculated upon a specific vibrational mode in both Stokes and anti-Stokes spectra through a Boltzmann distribution function (Equation (S5), Supporting Information). As shown in Figure 5c, the calculated vibrational temperatures of 4-MP adsorbates for a vibrational mode at 394, 635, and 1078 cm^{-1} are markedly elevated with respect to the phonon temperature of the RS-Au, MT-Au, and SC-Au nanocrystals under the 785 nm laser (Figure S21, Supporting Information), but they remain similar under the 633 nm laser (Figure S22, Supporting Information). The enhanced vibrational heating of strongly bound thiol adsorbates at longer excitation wavelength unambiguously confirms the involvement of direct charge transfer events, which also accounts for the elevated AQE in photocatalytic hydrolysis of AB above 730 nm. This may arise from the resonant excitation of the hybridized states of adsorbates as similarly observed over a methylene blue/Ag system,[9a,41] and the associated direct charge transfer across the adsorbate/metal interface would largely circumvent the energy loss due to electron–electron scattering.[42] Such a wavelength-dependent temperature difference between adsorbate and metal are less remarkable in MT-Au and SC-Au nanocrystals as shown in Figure 5c.

The hot electron dynamics on the adsorbate/metal system can be probed by TA spectroscopy using the pump–probe method. RS-Au and MT-Au as multiply-twinned nanocrystals are compared to identify the role of the asymmetric crystal shape of RS-Au. With a 650 nm pump pulse, a ground state bleach (GSB) band centered at 550 nm is observed in the TA data map of the 4-MP capped RS-Au nanocrystals (Figure 5d), which is attributed to the depletion of the plasmon electrons.[42] Similar GSB bands centered at 525 nm is observed
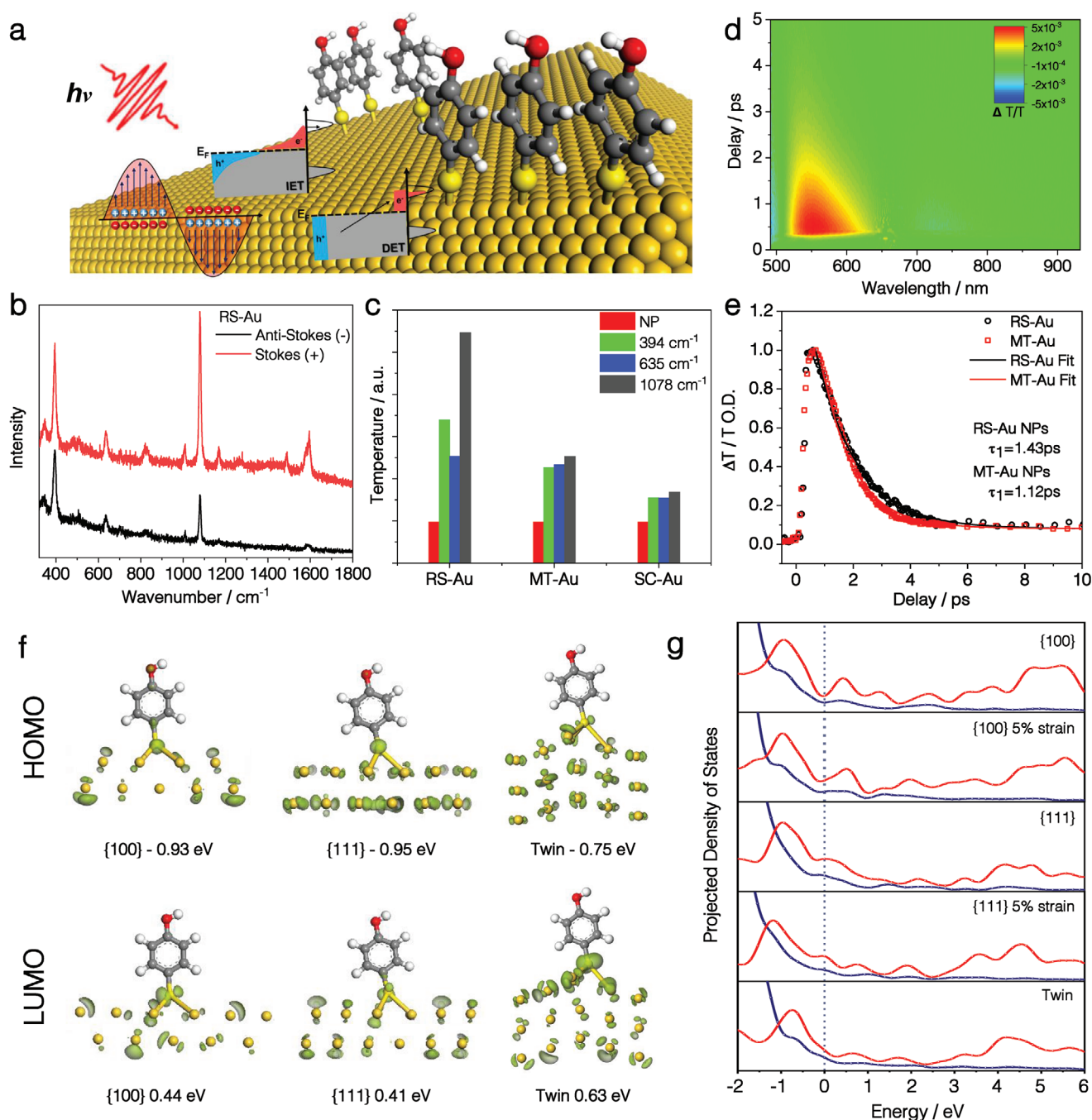
Figure 5. a) Schematic illustration of direct and indirect electron transfer pathways on Au surface with thiol adsorbates at different sites. b) Stokes and anti-Stokes Raman spectra of RS-Au at 785 nm excitation. c) Calculated temperature of three types of Au nanocrystals and their prominent vibrational modes (394, 635, and 1078 cm^{-1}) of 4-MP. d) 2D pseudocolor plot of TA spectra for RS-Au nanocrystals at 650 nm excitation. e) Bleach kinetics trace and corresponding fit of RS-Au and MT-Au at 650 nm excitation. f) The spatial distribution of HOMO and LUMO frontier orbitals for bonded 4-MP molecules on Au(100), Au(111) surfaces and a twinning boundary, respectively. g) Projected density of states for the p (red color) and d (navy color) components of S atom and Au binding sites underneath on Au(100), 5% strained Au(100), Au(111), and 5% strained Au(111) surfaces and the twin boundary sites, respectively.

for MT-Au nanocrystals, together with excited-state absorption (ESA) bands centered at 570 nm (Figure S23, Supporting Information). The plasmon bleach recovery time profiles probed at 550 and 525 nm for 4-MP capped RS-Au and MT-Au nanocrystals are shown in Figure 5e, which are characterized by two exponential functions attributed to the electron–phonon (e–ph) and phonon–phonon (ph–ph) scattering, respectively. The fitted lifetimes for both relaxation processes in these adsorbate/metal systems are $\tau_{e-ph} = 1.43/1.12$ ps and $\tau_{ph-ph} = 150.71/149.31$ ps, respectively (Figure S24, Supporting

Information). It has been reported that the lifetime of hot electrons is closely related with the surface chemistry,[43] crystal structure,[44] grain boundaries,[45] and environment.[46] The electron–phonon relaxation time $\tau_{e–ph}$ increases with increasing electronic heat capacity, but decreases with increasing electron–phonon coupling.[43] The prolonged $\tau_{e–ph}$ observed over the thiol capped RS-Au compared with the MT-Au nanocrystals is closely associated with the surface-chemistry induced CIS that effectively retards the internal thermalization process,[47] and arises from the more pronounced increase of electronic heat capacity than electron–phonon coupling due to the introduced adsorbate states near Fermi level.[43] Actually, the modulation of these adsorbate states has been reported to effectively tune the CID and thus the efficiency of plasmonic hot-electron energy transfer.[36] We further investigate the electronic structure and these near Fermi-level states in the Au–thiol system by employing DFT calculations, with an emphasis on the effects of surface facets, strain, and twin boundary that appear in RS-Au, MT-Au, and SC-Au nanocrystals. As Figure S25 in the Supporting Information shows, the derived d-band center values shift closer to the Fermi level in the order of strained {100}, strained {111}, {100}, {111}, twin boundary, which leads to a decreased filling of metal–adsorbate antibonding states and stronger binding of adsorbate molecules. Specifically, the 4-MP molecules preferentially adsorb on the fourfold hollow sites of the {100} surface and threefold hollow sites of {111} surface or twin boundary with a slightly distorted geometry (Figure 5f). The strong chemical bonding between Au and S atoms in these Au–thiol system produces hybridized surface states near Fermi level that opens up a greatly reduced energy gap between the frontier states (e.g., 1.37 eV for thiol molecular on Au {100}) compared with that of free-standing thiol molecules (4.68 eV).[38b] These frontier states for diverse Au–thiol geometries are mainly contributed by Au 5d and S 3p states and can be clearly visualized by the projected density of states (PDOS) onto the S atom and Au binding sites underneath as shown in Figure 5g. Combined with the spatial distribution of molecular orbitals (MOs) associated with these similar states (Figure 5f; Figure S26, Supporting Information), the occupied frontier states (HOMO) (e.g., −0.93 eV for thiol molecular on Au{100} and −0.95 eV for thiol molecular on Au{111}) are composed of Au 5d and lone-pair type p orbitals localized on S atom with a nonbonding character (n-type), while the unoccupied frontier states (LUMO) (e.g., 0.44 eV for thiol molecular on Au{100} and 0.41 eV for thiol molecular on Au{111}) contain much less d states from the metal substrate but predominantly σ^*-type antibonding orbital formed between Au d_{z^2} and S p_z orbitals. Such an electronic structure allows the efficient n→ σ^* type direct electronic excitation between the frontier states with a small energy gap, which accounts for the observed elevation of photocatalytic activity at longer wavelength (> 730 nm) of the SPR bands for RS-Au nanocrystals. On the other side, the diminished metal d states in the unoccupied region allow the isolation of electron-accepting states from the metal substrate, which may extend the lifetime of excited states toward efficient photochemical reactions.[38b] More importantly, we note in this work that the direct electronic excitation pathway is significantly affected by the microstructure of Au nanocrystals, as the {100} facets

would create more pronounced unoccupied density of states for greater electronic excitation probability in the Au–thiol system than {111} facets and twin boundary. In addition, the tensile strain on {100} facets would further increase the energy gap by 0.11 eV between these hybridized surface states. These facts unambiguously demonstrate that by tailoring the microstructure of plasmonic metal nanocrystals, both the efficiency and resonant energy of the direct electronic transition between hybridized surface states can be readily modulated. The proposed n→ σ^* type direct electronic transition in the Au–thiol system would facilitate the photodissociation of Au−S σ-bond possibly through vibration energy accumulation,[42] which produces activated 4-MP species (*SPhOH) that subsequently initiate the full cycle of AB hydrolysis reaction as schematically illustrated in Figure 4a. The RS-Au nanocrystals that adopt a unique surface termination including {100} facets would thus benefit from enhanced direct electronic excitation in contrast to the indirect electron transfer, though the quantitative discrimination between individual pathways remains challenging.

3. Conclusion

Monometallic Au nanocrystals with reduced symmetry were rationally designed and artificially created via wet-chemical synthesis through a COUD strategy assisted by both ionic additive and thiol passivator. The underlying microscopic mechanism of symmetry-breaking crystal growth beyond the ECS is unraveled by electron microscopy and microanalysis, which is initiated by the site-specific defect nucleation followed with nonepitaxial growth mode. The unique asymmetric shape of Au nanocrystals leads to broadband SPR optical properties, while their microstructures including surface facets, strain, and twin boundary are closely related with the hot carrier generation and transfer mechanisms in the metal–adsorbate system, as evidenced by combined steady-state/dynamic spectroscopic characterizations and theoretical calculations. Both factors largely restrict the efficiency of photochemical reactions. Targeting at efficient solar energy harvesting via plasmon-enhanced photocatalysis, this work demonstrates that a precise chemical control of both size/shape and microstructures of metallic nanocrystals offers not only large and tunable absorption cross-section of nanocrystals but also alteration between the competitive direct and indirect hot carrier transfer pathways across the metal–adsorbate interface.

Supporting Information

Supporting Information is available from the Wiley Online Library or from the author.

Conflict of Interest

The authors declare no conflict of interest.

Keywords

[1] a) Y. Xia, Y. Xiong, B. Lim, S. E. Skrabalak, *Angew. Chem., Int. Ed.* **2009**, *48*, 60; b) H. Ataee-Esfahani, K. M. Koczkur, R. G. Weiner, S. E. Skrabalak, *ACS Omega* **2018**, *3*, 3952; c) X. Wang, Y. Zhu, A. Vasileff, Y. Jiao, S. Chen, L. Song, B. Zheng, Y. Zheng, S. Qiao, *ACS Energy Lett.* **2018**, *3*, 1198; d) J. Huang, Y. Zhu, C. Liu, Z. Shi, A. Fratalocchi, Y. Han, *Nano Lett.* **2016**, *16*, 617; e) Z. Zhang, G. Liu, X. Cui, B. Chen, Y. Zhu, Y. Gong, F. Saleem, S. Xi, Y. Du, A. Borgna, Z. Lai, Q. Zhang, B. Li, Y. Zong, Y. Han, L. Gu, H. Zhang, *Adv. Mater.* **2018**, *30*, 1801741; f) D. J. Martin, P. J. T. Reardon, S. J. A. Moniz, J. Tang, *J. Am. Chem. Soc.* **2014**, *136*, 12568; g) Q. Chen, T. Cheng, H. Fu, Y. Zhu, *Chin. J. Catal.* **2019**, *40*, 1035; h) Y. Zhu, J. He, C. Shang, X. Miao, J. Huang, Z. Liu, H. Chen, Y. Han, *J. Am. Chem. Soc.* **2014**, *136*, 12746.

[2] J. Yan, Y. Chen, S. Hou, J. Chen, D. Meng, H. Zhang, H. Fan, Y. L. Ji, X. Wu, *Nanoscale* **2017**, *9*, 11093.

[3] a) R. Narayanan, M. A. El-Sayed, *J. Phys. Chem. B* **2005**, *109*, 12663; b) A. Zecchina, E. Groppo, S. Bordiga, *Chem. - Eur. J.* **2007**, *13*, 2440.

[4] K. L. Kelly, E. Coronado, L. L. Zhao, G. C. Schatz, *J. Phys. Chem. B* **2003**, *107*, 668.

[5] B. J. Wiley, S. H. Im, Z. Y. Li, J. McLellan, A. Siekkinen, Y. Xia, *J. Phys. Chem. B* **2006**, *110*, 15666.

[6] a) K. Nakayama, K. Tanabe, H. A. Atwater, *Appl. Phys. Lett.* **2008**, *93*, 121904; b) A. Tanaka, K. Hashimoto, H. Kominami, *J. Am. Chem. Soc.* **2012**, *134*, 14526; c) F. X. Xiao, B. Liu, *Adv. Mater. Interfaces* **2018**, *5*, 1701098; d) X. C. Dai, M. H. Huang, Y. B. Li, T. Li, S. Hou, Z. Q. Wei, F. X. Xiao, *J. Phys. Chem. C* **2020**, *124*, 4989.

[7] a) M. J. Kale, T. Avanesian, P. Christopher, *ACS Catal.* **2014**, *4*, 116; b) S. Mukherjee, F. Libisch, N. Large, O. Neumann, L. V. Brown, J. Cheng, J. B. Lassiter, E. A. Carter, P. Nordlander, N. J. Halas, *Nano Lett.* **2013**, *13*, 240.

[8] a) M. L. Brongersma, N. J. Halas, P. Nordlander, *Nat. Nanotechnol.* **2015**, *10*, 25; b) P. Christopher, M. Moskovits, *Annu. Rev. Phys. Chem.* **2017**, *68*, 379; c) A. O. Govorov, H. Zhang, Y. K. Gun'ko, *J. Phys. Chem. C* **2013**, *117*, 16616; d) K. Y. Jiang, X. C. Dai, Y. Yu, Q. L. Mo, F. X. Xiao, *J. Phys. Chem. C* **2018**, *122*, 12291.

[9] a) C. Boerigter, R. Campana, M. Morabito, S. Linic, *Nat. Commun.* **2016**, *7*, 10545; b) C. Boerigter, U. Aslam, S. Linic, *ACS Nano* **2016**, *10*, 6108.

[10] M. Fialkowski, K. J. M. Bishop, R. Klajn, S. K. Smoukov, C. J. Campbell, B. A. Grzybowski, *J. Phys. Chem. B* **2006**, *110*, 2482.

[11] A. Furube, L. Du, K. Hara, R. Katoh, M. Tachiya, *J. Am. Chem. Soc.* **2007**, *129*, 14852.

[12] C. Bauer, J. P. Abid, D. Fermin, H. H. Girault, *J. Chem. Phys.* **2004**, *120*, 9302.

[13] a) C. T. Campbell, S. C. Parker, D. E. Starr, *Science* **2002**, *298*, 811; b) M. Valden, X. Lai, D. W. Goodman, *Science* **1998**, *281*, 1647.

[14] H. Huang, L. Zhang, Z. Lv, R. Long, C. Zhang, Y. Ling, K. Wei, C. Wang, L. Chen, Z. Y. Li, Q. Zhang, Y. Luo, Y. Xiong, *J. Am. Chem. Soc.* **2016**, *138*, 6822.

[15] a) E. Gonzalez, J. Arbiol, V. F. Puntes, *Science* **2011**, *334*, 1377; b) Y. Feng, Y. Wang, J. He, X. Song, Y. Y. Tay, H. H. Hng, X. Y. Ling, H. Chen, *J. Am. Chem. Soc.* **2015**, *137*, 7624; c) X. Lan, Q. Wang, *ACS Appl. Mater. Interfaces* **2016**, *8*, 34598.

[16] a) G. Wulff, *Z. Kristallogr. - Cryst. Mater.* **1901**, *34*, 449; b) Y. Sun, Y. Xia, *Science* **2002**, *298*, 2176.

[17] a) H. Wang, Y. Wu, B. Lassiter, C. L. Nehl, J. H. Hafner, P. Nordlander, N. J. Halas, *Proc. Natl. Acad. Sci. USA* **2006**, *103*, 10856; b) J. Sancho-Parramon, D. Jelovina, *Nanoscale* **2014**, *6*, 13555.

[18] E. Ye, K. Y. Win, H. R. Tan, M. Lin, C. P. Teng, A. Mlayah, M. Y. Han, *J. Am. Chem. Soc.* **2011**, *133*, 8506.

[19] a) Y. Xia, P. Yang, Y. Sun, Y. Wu, B. Mayers, B. Gates, Y. Yin, F. Kim, Y. Yan, *Adv. Mater.* **2003**, *15*, 353; b) E. Jeong, K. Kim, I. Choi, S. Jeong, Y. Park, H. Lee, S. H. Kim, L. P. Lee, Y. Choi, T. Kang, *Nano Lett.* **2012**, *12*, 2436.

[20] a) J. B. Lassiter, M. W. Knight, N. A. Mirin, N. J. Halas, *Nano Lett.* **2009**, *9*, 4326; b) J. C. Love, B. D. Gates, D. B. Wolfe, K. E. Paul, G. M. Whitesides, *Nano Lett.* **2002**, *2*, 891; c) D. Pornpattananangkul, L. Zhang, S. Olson, S. Aryal, M. Obonyo, K. Vecchio, C. M. Huang, L. Zhang, *J. Am. Chem. Soc.* **2011**, *133*, 4132; d) J. Ye, N. Verellen, W. Van Roy, L. Lagae, G. Maes, G. Borghs, P. Van Dorpe, *ACS Nano* **2010**, *4*, 1457.

[21] a) X. Ye, L. Jin, H. Caglayan, J. Chen, G. Xing, C. Zheng, V. Doan-Nguyen, Y. Kang, N. Engheta, C. R. Kagan, C. B. Murray, *ACS Nano* **2012**, *6*, 2804; b) X. Ye, C. Zheng, J. Chen, Y. Gao, C. B. Murray, *Nano Lett.* **2013**, *13*, 765; c) B. Nikoobakht, M. A. El-Sayed, *Chem. Mater.* **2003**, *15*, 1957.

[22] X. Huang, S. Li, Y. Huang, S. Wu, X. Zhou, S. Li, C. L. Gan, F. Boey, C. A. Mirkin, H. Zhang, *Nat. Commun.* **2011**, *2*, 292.

[23] a) S. E. Habas, H. Lee, V. Radmilovic, G. A. Somorjai, P. Yang, *Nat. Mater.* **2007**, *6*, 692; b) G. Du, J. Pei, Z. Jiang, Q. Chen, Z. Cao, Q. Kuang, Z. Xie, L. Zheng, *Sci. Bull.* **2018**, *63*, 892; c) Z. Wang, Z. Chen, H. Zhang, Z. Zhang, H. Wu, M. Jin, C. Wu, D. Yang, Y. Yin, *ACS Nano* **2015**, *9*, 3307.

[24] J. Zhang, D. J. Xue, X. Zhan, Z. Li, D. Zeng, H. Song, *ACS Appl. Mater. Interfaces* **2017**, *9*, 27102.

[25] F. Maillard, G. Q. Lu, A. Wieckowski, U. Stimming, *J. Phys. Chem. B* **2005**, *109*, 16230.

[26] D. G. de Oteyza, E. Barrena, Y. Zhang, T. N. Krauss, A. Turak, A. Vorobiev, H. Dosch, *J. Phys. Chem. C* **2009**, *113*, 4234.

[27] Y. Feng, J. He, H. Wang, Y. Y. Tay, H. Sun, L. Zhu, H. Chen, *J. Am. Chem. Soc.* **2012**, *134*, 2004.

[28] a) C. L. Aravinda, S. M. Mayanna, V. S. Muralidharan, *Proc. Indian Acad. Sci.* **2000**, *112*, 543; b) O. Cavalleri, S. E. Gilbert, K. Kern, *Surf. Sci.* **1997**, *377*, 931; c) E. Herrero, L. J. Buller, H. D. Abruna, *Chem. Rev.* **2001**, *101*, 1897.

[29] C. L. Johnson, E. Snoeck, M. Ezcurdia, B. Rodriguez-Gonzalez, I. Pastoriza-Santos, L. M. Liz-Marzan, M. J. Hytch, *Nat. Mater.* **2008**, *7*, 120.

[30] J. Wu, L. Qi, H. You, A. Gross, J. Li, H. Yang, *J. Am. Chem. Soc.* **2012**, *134*, 11880.

[31] S. Jo, P. Verma, Y. Kuwahara, K. Mori, W. Choi, H. Yamashita, *J. Mater. Chem. A* **2017**, *5*, 21883.

[32] a) A. O. Govorov, H. H. Richardson, *Nano Today* **2007**, *2*, 30; b) R. Kamarudheen, G. Kumari, A. Baldi, *Nat. Commun.* **2020**, *11*, 3957.

[33] J. W. Hong, D. H. Wi, S. U. Lee, S. W. Han, *J. Am. Chem. Soc.* **2016**, *138*, 15766.

[34] C. Hu, X. Chen, J. Jin, Y. Han, S. Chen, H. Ju, J. Cai, Y. Qiu, C. Gao, C. Wang, Z. Qi, R. Long, L. Song, Z. Liu, Y. Xiong, *J. Am. Chem. Soc.* **2019**, *141*, 7807.

[35] M. J. Kale, T. Avanesian, H. Xin, J. Yan, P. Christopher, *Nano Lett.* **2014**, *14*, 5405.

[36] S. Y. Lee, P. V. Tsalu, G. W. Kim, M. J. Seo, J. W. Hong, J. W. Ha, *Nano Lett.* **2019**, *19*, 2568.

[37] P. Christopher, H. L. Xin, A. Marimuthu, S. Linic, *Nat. Mater.* **2012**, *11*, 1044.

[38] a) L. Kang, Y. Guo, P. Miao, M. Sun, B. Song, P. Xu, X. Liu, *Eur. J. Inorg. Chem.* **2019**, *1*, 23; b) E. Kazuma, J. Jung, H. Ueba, M. Trenary, Y. Kim, *J. Am. Chem. Soc.* **2017**, *139*, 3115.

[39] R. C. Maher, C. M. Galloway, E. C. Le Ru, L. F. Cohena, P. G. Etchegoin, *Chem. Soc. Rev.* **2008**, *37*, 965.

[40] a) E. B. Brauns, C. J. Murphy, M. A. Berg, *J. Am. Chem. Soc.* **1998**, *120*, 2449; b) D. P. dos Santos, M. L. A. Temperini, A. G. Brolo, *J. Am. Chem. Soc.* **2012**, *134*, 13492.

[41] a) Y. Y. Cai, E. Sung, R. Zhang, L. J. Tauzin, J. G. Liu, B. Ostovar, Y. Zhang, W. S. Chang, P. Nordlander, S. Link, *Nano Lett.* **2019**, *19*, 1067; b) A. Carattino, M. Caldarola, M. Orrit, *Nano Lett.* **2018**, *18*,

874; c) C. Steuwe, C. F. Kaminski, J. J. Baumberg, S. Mahajan, *Nano Lett.* **2011**, *11*, 5339.

[42] Y. Zhang, S. He, W. Guo, Y. Hu, J. Huang, J. R. Mulcahy, W. D. Wei, *Chem. Rev.* **2018**, *118*, 2927.

[43] K. O. Aruda, M. Tagliazucchi, C. M. Sweeney, D. C. Hannah, G. C. Schatz, E. A. Weiss, *Proc. Natl. Acad. Sci. USA* **2013**, *110*, 4212.

[44] Y. Tang, M. Ouyang, *Nat. Mater.* **2007**, *6*, 754.

[45] S. Link, C. Burda, Z. L. Wang, M. A. El-Sayed, *J. Chem. Phys.* **1999**, *111*, 1255.

[46] S. Link, D. J. Hathcock, B. Nikoobakht, M. A. El-Sayed, *Adv. Mater.* **2003**, *15*, 393.

[47] C. Bauer, J. P. Abid, H. H. Girault, *J. Phys. Chem. B* **2006**, *110*, 4519.

[48] L. Wang, H. L. Li, W. Zhang, X. Zhao, J. Qiu, A. Li, X. Zheng, Z. Hu, R. Si, J. Zeng, *Angew. Chem., Int. Ed.* **2017**, *56*, 4712.